

# Highly efficient optical detection of surface-generated fluorescence

Jörg Enderlein, Thomas Ruckstuhl, and Stefan Seeger

We present a theoretical study of a new highly efficient system for optical light collection, designed for ultrasensitive fluorescence detection of surface-bound molecules. The main core of the system is a paraboloid glass segment acting as a mirror for collecting the fluorescence. A special feature of the system is its ability to sample not only fluorescence that is emitted below the angle of total internal reflection (the critical angle) but also particularly the light above the critical angle. As shown, this is especially advantageous for collecting the fluorescence of surface-bound molecules. A comparison is made with conventional high-aperture microscope objectives. Furthermore, it is shown that the system allows not only for highly efficient light collection but also for confocal imaging of the detection region, which is of great importance for rejecting scattered light in potential applications such as the detection of only a few molecules. © 1999 Optical Society of America

*OCIS codes:* 080.2740, 110.0180, 120.1880, 170.2520.

## 1. Introduction

In many fields of chemical and biochemical analyses, the method of laser-induced fluorescence detection plays an extraordinarily important role. In most applications a sample with a fluorescently tagged analyte is excited by a laser beam, and the emitted fluorescence is optically collected and electro-optically detected by a suitable detection system. Usually, the intensity of the detected fluorescence is then used for determining analyte concentrations. Other fluorescence characteristics of the analyte, such as fluorescence lifetime, may also be used for inferring sample characteristics influencing the analyte's fluorescence behavior.

A central issue in all these applications is the ratio of the fluorescence signal to the background signal. The origins of the background signal may be manifold: For ultrasensitive fluorescence detection (very small analyte concentrations, of the order of or smaller than  $10^{-13}$  M) the main source of background is the Rayleigh and the Raman scattering of the exciting laser beam by the sample. Other sources of

background are sample contamination by fluorescing nonanalyte substances and thermoelectric noise of the detection electronics. To improve the signal-to-background ratio, one may increase the signal or/and reduce the background. The latter is usually done by spatially restricting the detection to a small detection volume (spatial filtering as in confocal microscopy) by use of highly efficient optical filters for scattered light rejection (spectral filtering) and by reduction of the internal noise of the detection electronics (e.g., by cooling). More sophisticated methods also use time filtering, employing the fact that after a sufficiently short pulse of laser excitation the decay of the analyte fluorescence is usually much longer (1–10 ns) than the decay of the light scattering ( $\sim 10^2$  ps).

To increase the signal, one must improve the detection efficiency of the fluorescence light. An obvious way is to use highly sensitive electro-optical detectors, such as single-photon avalanche diodes that reach quantum yields of detection as high as 0.8. A technically more difficult problem is to improve the purely optical part of the detection system. In common epifluorescence microscopes, high-quality microscope objectives with numerical apertures as high as possible are used for collecting the fluorescence emission (those as high as 1.6 are commercially available). However, increasing the numerical aperture (NA) leads to more and more complicated multiple-lens systems with increasing optical losses due to multiple interfaces.

---

The authors are with the Institute of Analytical Chemistry, Chemo- und Biosensors, University of Regensburg, PF 10 10 42, D-93040 Regensburg, Germany.

Received 13 July 1998; revised manuscript received 3 November 1998.

0003-6935/99/040724-09\$15.00/0

© 1999 Optical Society of America

The problem of improving the pure optical collection efficiency of the fluorescence light becomes more intricate in the case of surface-bound molecules. It has long been known that molecules positioned at interfaces, constituting a discontinuity in refractive index, emit the greater part of their fluorescence into the medium with a higher refractive index.<sup>1,2</sup> In many fluorescence-detection experiments, where molecules are deposited onto a glass substrate (coverslip) from a liquid solution, this effect improves the efficiency of the fluorescence light collection. But little attention is usually given to the angular distribution of the fluorescence emission of the surface-bound molecules. This distribution differs significantly from that of the emission of free molecules in an homogeneous medium. For molecules situated at refractive-index discontinuities the emission maximum lies at an angle of total internal reflection (the critical angle) of the two media, and a significant part of the radiation is emitted at angles above the critical angle (so-called evanescent modes or forbidden light). However, this angular region is covered only by high-aperture objectives (NA > 1.33 for a water solution).

In the present paper we propose a new optical-detection system for highly sensitive fluorescence detection of surface-bound fluorophores. The core of the system is a glass element in the shape of a segment of a paraboloid of revolution that serves two purposes. First, by providing a high refractive medium, it increases the fluorescence emission of molecules on its surface into the paraboloid segment. Second, the parabolic shape of the element acts as a mirror (through total internal reflection) that collects the fluorescence light, preferably around the angles of maximum emission. A similar setup, in which a metallic elliptic mirror was used, was employed by Hecht *et al.*<sup>3</sup> in a special configuration of a scanning near-field microscope. There the mirror also served the purpose of collecting evanescent light modes, i.e., radiation above the critical angle. But the main reason for collecting this radiation there was not to increase the collection efficiency but to improve the spatial resolution and image contrast of the scanning near-field microscope and to gain information about the angular distribution of radiation excited by the near-field probe.

In Section 2 we recall briefly the theory of light emission of a dipole near a refractive-index discontinuity. In Section 3 we describe the paraboloid light collector and calculate its light-collection characteristics. In Section 4 we present ray-tracing calculations for a paraboloid plus lens system, showing the possibility of achieving confocal imaging, which is important for efficient suppression of scattered light.

## 2. Radiation of a Dipole near a Surface

Below we consider a fluorescing molecule within a completely classical electrodynamic framework as a radiating electric dipole. To derive the radiation characteristics of an oscillating electric dipole over a surface, we employ a method that is different from

the usual Hertz vector approach,<sup>4</sup> but we start with an integral representation of the radiation of a free electric dipole. We assume that the dipole is oscillating with angular frequency  $\omega$  and for all variables (dipole moment, electric, and magnetic field) a time dependence of the kind  $\exp(-i\omega t)$ .

Then the complex amplitude of the electric field  $\mathbf{E}_D$  at position  $\mathbf{r}$  of an oscillating dipole with dipole amplitude  $\mathbf{p}$  at position  $\mathbf{r}_0$  within a homogeneous medium with dielectric constant  $\epsilon_1$  is given, in a coordinate-free notation, by the integral<sup>5</sup>

$$\mathbf{E}_D(\mathbf{r}) = \frac{1}{\epsilon_1} \int \frac{d^3\mathbf{k}}{2\pi^2} [\mathbf{k}^2\mathbf{p} - \mathbf{k}(\mathbf{k} \cdot \mathbf{p})] \frac{\exp(i\mathbf{k} \cdot \mathbf{R})}{k_1^2 - k^2}, \quad (1)$$

where  $c$  is the speed of light and  $\mathbf{R} = \mathbf{r} - \mathbf{r}_0$ ,  $k_1 = \sqrt{\epsilon_1} \omega/c$ . The integration extends over the whole three-dimensional  $\mathbf{k}$  space with  $d^3\mathbf{k}$  denoting an infinitesimally small volume element of this space. Equation (1) is just the plane-wave representation of the electric field of the oscillating dipole. By integrating along a fixed direction (denoted as the  $z$  direction) of the three-dimensional  $\mathbf{k}$  space, one arrives at

$$\mathbf{E}_D = \frac{i}{2\pi\epsilon_1} \int \frac{d^2\mathbf{q}}{w_1} [k_1^2\mathbf{p} - \mathbf{k}_1(\mathbf{k}_1 \cdot \mathbf{p})] \exp[i\mathbf{q} \cdot (\boldsymbol{\rho} - \boldsymbol{\rho}_0) + iw_1|z - z_0|], \quad (2)$$

where we used the abbreviations  $\mathbf{R} = (\boldsymbol{\rho} - \boldsymbol{\rho}_0, z - z_0)$ ,  $\mathbf{k}_1 = (\mathbf{q}, \pm w_1)$ , and  $w_1 = (k_1^2 - q^2)^{1/2}$ . Thus  $\boldsymbol{\rho} - \boldsymbol{\rho}_0$  and  $\mathbf{q}$  are the vector parts of  $\mathbf{R}$  and  $\mathbf{k}_1$  perpendicular to the  $z$  direction. In the definition of  $\mathbf{k}_1$  the positive sign in front of  $w_1$  relates to  $z > z_0$  and the negative sign to  $z < z_0$ . The value of  $w_1$  is assumed to always have a zero or a positive imaginary part.

Equation (2) is the so-called Weyl representation.<sup>6</sup> This representation is perfectly suited for deriving the electric field of the dipole (at  $z = z_0 > 0$ ) over a surface defined by  $z = 0$ . Every plane wave in the Weyl representation is refracted and diffracted according to Fresnel's formulas. If the medium at  $z < 0$  has dielectric constant  $\epsilon_2$ , the reflection and the transmission coefficients for plane  $p$  and  $s$  waves with wave vector  $\mathbf{k}_1 = (\mathbf{q}, -w_1)$  are given by<sup>7</sup>

$$R_p = \frac{w_1\epsilon_2 - w_2\epsilon_1}{w_1\epsilon_2 + w_2\epsilon_1}, \quad R_s = \frac{w_1 - w_2}{w_1 + w_2}, \quad (3)$$

$$T_p = \frac{2n_1n_2w_1}{w_1\epsilon_2 + w_2\epsilon_1}, \quad T_s = \frac{2w_1}{w_1 + w_2}, \quad (4)$$

where  $w_2 = (k_2^2 - q^2)^{1/2}$ ,  $k_2 = n_2\omega/c$ ,  $n_{1,2} = \sqrt{\epsilon_{1,2}}$ .

It remains to separate the  $p$  and  $s$  waves within the general Weyl representation. By direct substitution it can be shown that the following equation holds for  $\mathbf{k}_1 = (\mathbf{q}, -w_1)$ :

$$\mathbf{k}_1 \otimes \mathbf{k}_1 - \mathbf{k}_1^2 \hat{\mathbf{I}} = k_1^2 (\hat{\mathbf{k}}_{p1} \otimes \hat{\mathbf{k}}_{p1} + \hat{\mathbf{k}}_s \otimes \hat{\mathbf{k}}_s), \quad (5)$$

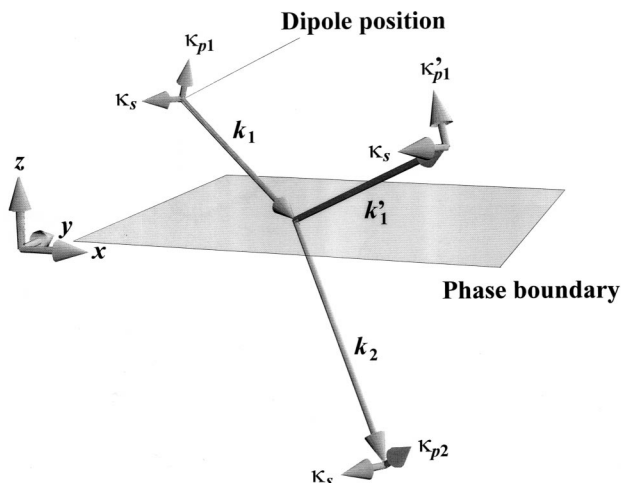


Fig. 1. Geometry of the reflected and transmitted electromagnetic field at the phase boundary dividing regions of different refractive index.

where  $\hat{I}$  is the unit matrix, and the unit vectors  $\hat{\kappa}_{p1}$  and  $\hat{\kappa}_s$  are given by

$$\hat{\kappa}_{p1} = \frac{1}{k_1} (w_1 \hat{q}, q), \quad \hat{\kappa}_s = (\hat{z} \times \hat{q}, 0), \quad (6)$$

where  $\hat{q}$  and  $\hat{z}$  are unit vectors along  $\mathbf{q}$  and the  $z$  axis, respectively (see Fig. 1). Thus, for  $z < z_0$ ,  $\mathbf{k}_1 = (\mathbf{q}, -w_1)$ , Eq. (12) can be rewritten as

$$\mathbf{E}_D = \frac{ik_1^2}{2\pi\epsilon} \int \frac{d^2\mathbf{q}}{w_1} [\hat{\kappa}_{p1}(\hat{\kappa}_{p1} \cdot \mathbf{p}) + \hat{\kappa}_s(\hat{\kappa}_s \cdot \mathbf{p})] \times \exp[i\mathbf{q} \cdot (\mathbf{p} - \mathbf{p}_0) + iw_1|z - z_0|]. \quad (7)$$

The unit vectors  $\hat{\kappa}_{p1}$  and  $\hat{\kappa}_s$  are the polarization unit vectors of  $p$  and  $s$  waves with respect to the plane  $z = 0$ . It is now obvious how to obtain the contribution of the reflected field to the complete dipole field amplitude:

$$\mathbf{E}_R = \frac{ik_1^2}{2\pi\epsilon} \int \frac{d^2\mathbf{q}}{w_1} [\hat{\kappa}_{p1}' R_p(\hat{\kappa}_{p1}' \cdot \mathbf{p}) + \hat{\kappa}_s R_s(\hat{\kappa}_s \cdot \mathbf{p})] \times \exp[i\mathbf{q} \cdot (\mathbf{p} - \mathbf{p}_0) + iw_1(z + z_0)], \quad (8)$$

where the additional unit vector

$$\hat{\kappa}_{p1}' = \frac{1}{k_1} (-w_1 \hat{q}, q) \quad (9)$$

was introduced (see Fig. 1).

Equivalently, the transmitted field amplitude is given by ( $z < 0$ )

$$\mathbf{E}_T = \frac{ik_1^2}{2\pi\epsilon} \int \frac{d^2\mathbf{q}}{w_1} [\hat{\kappa}_{p2} T_p(\hat{\kappa}_{p1} \cdot \mathbf{p}) + \hat{\kappa}_s T_s(\hat{\kappa}_s \cdot \mathbf{p})] \times \exp[i\mathbf{q} \cdot (\mathbf{p} - \mathbf{p}_0) + iw_1 z_0 + iw_2 |z|], \quad (10)$$

where the unit vector  $\hat{\kappa}_{p2}$  is given by (see Fig. 1)

$$\hat{\kappa}_{p2} = \frac{1}{k_2} (w_2 \hat{q}, q), \quad (11)$$

with  $w_2 = (k_2^2 - q^2)^{1/2}$ ,  $\text{Re}(w_2) \geq 0$ ,  $\text{Im}(w_2) \geq 0$ . (Transmitted waves are always propagating along the negative  $z$  direction.)

The flux intensity  $\mathbf{S}$  of electromagnetic radiation is given by the Poynting vector  $\mathbf{S}$ :

$$\mathbf{S} = \frac{c}{8\pi} \text{Re}(\mathbf{E}^* \times \mathbf{B}). \quad (12)$$

For the free dipole, Eq. (10), we have for the radiation flux into a solid angle  $d\Omega^2$  along  $\mathbf{k}_1$

$$\begin{aligned} \frac{d^2 S}{d\Omega^2} &= \frac{c}{8\pi\epsilon_1^2} \left| [k_1^2 \mathbf{p} - \mathbf{k}_1(\mathbf{k}_1 \cdot \mathbf{p})] \times \left\{ \frac{c\mathbf{k}_1}{\omega} \times [k_1^2 \mathbf{p} \right. \right. \\ &\quad \left. \left. - \mathbf{k}_1(\mathbf{k}_1 \cdot \mathbf{p}) \right\} \right|^2 \\ &= \frac{ck_0^2}{8\pi n_1} [k_1^2 p^2 - (\mathbf{k}_1 \cdot \mathbf{p})^2], \end{aligned} \quad (13)$$

where  $k_0 = \omega/c$  is the wave vector in vacuum. If the dipole is oriented, e.g., along the  $z$  axis, and the angle between  $\mathbf{k}_1 \|\mathbf{r}$  and  $\hat{z}$  is denoted by  $\theta$ , Eq. (13) yields

$$\frac{dS}{d\theta} = \frac{cn_1 k_0^4 p^2}{8\pi} \sin^2 \theta, \quad (14)$$

and the total radiation in all directions is given by

$$2\pi \int_0^\pi d\theta \sin \theta \frac{dS}{d\theta} = \frac{1}{3} cn_1 k_0^4 p^2. \quad (15)$$

For a propagating plane wave,  $\mathbf{E} \exp(i\mathbf{k}_1 \cdot \mathbf{r})$ , the flux intensity of electromagnetic radiation in the direction of  $\mathbf{k}_1$  is given by

$$S = \frac{cn_1}{8\pi} |\mathbf{E}|^2.$$

thus the flux intensity of the dipole radiation emitted into the positive semispace ( $z > 0$ ) into a solid angle element  $d\Omega_1^2$  in direction  $(\mathbf{q}, w_1)$ ,  $\text{Re}(w_1) > 0$ ,  $\text{Im}(w_1) = 0$ , will be proportional to

$$\begin{aligned} \frac{d^2 S_1}{d\Omega_1^2} &= C_1 n_1 \left| \frac{k_1^3}{2\pi\epsilon_1} \right|^2 |\hat{\kappa}_{p1}'(\hat{\kappa}_{p1}' \cdot \mathbf{p}) + \hat{\kappa}_{p1}' R_p \exp(i2w_1 z_0) \\ &\quad \times (\hat{\kappa}_{p1} \cdot \mathbf{p}) + \hat{\kappa}_s [1 + R_s \exp(i2w_1 z_0)](\hat{\kappa}_s \cdot \mathbf{p})|^2 \\ &= C_1 n_1 \left| \frac{k_1^3}{2\pi\epsilon_1} \right|^2 \{ |[\hat{\kappa}_{p1}' + R_p \exp(i2w_1 z_0) \hat{\kappa}_{p1}] \cdot \mathbf{p}|^2 \\ &\quad + |[1 + R_s \exp(i2w_1 z_0)](\hat{\kappa}_s \cdot \mathbf{p})|^2 \}. \end{aligned} \quad (16)$$

Here  $C$  denotes a proportionality constant. In deriving Eq. (16), we have taken into account that

$$\frac{d^2 \mathbf{q}}{w_1 k_1} = d\Omega_1^2. \quad (17)$$

One can determine the constant  $C$  by noting that Eq. (16) has to transform into Eq. (13) in the case of equal values of  $\epsilon_1$  and  $\epsilon_2$ . Then  $R_p = R_s = 0$ , and one obtains

$$C_1 n_1 \frac{k_1^4}{4\pi^2 \epsilon_1^2} = \frac{ck_0^2}{8\pi n_1} \quad (18)$$

or

$$C_1 = \frac{\pi c}{2k_1^2}. \quad (19)$$

Analogously, the flux intensity distribution into the negative semispace ( $z < 0$ ) into solid angle element  $d\Omega_2^2$  in direction  $(\mathbf{q}, w_2)$ ,  $\text{Re}(w_2) < 0$ ,  $\text{Im}(w_2) = 0$ , is given by

$$\begin{aligned} \frac{d^2 S_2}{d\Omega_2^2} = C_2 n_2 \left[ \frac{k_1^2 k_2 w_2}{2\pi \epsilon_1 w_1} \right]^2 \{ |T_p \hat{\mathbf{k}}_{p1} \cdot \mathbf{p}|^2 + |T_s \hat{\mathbf{k}}_s \cdot \mathbf{p}|^2 \} \\ \times \exp[-2 \text{Im}(w_1) z_0], \end{aligned} \quad (20)$$

where  $C_2$  can be found to be analogous to  $C_1$ ,

$$C_2 = \frac{\pi c}{2k_2^2}, \quad (21)$$

and the solid angle element is given by

$$d\Omega_2^2 = \frac{d^2 \mathbf{q}}{k_2 w_2}. \quad (22)$$

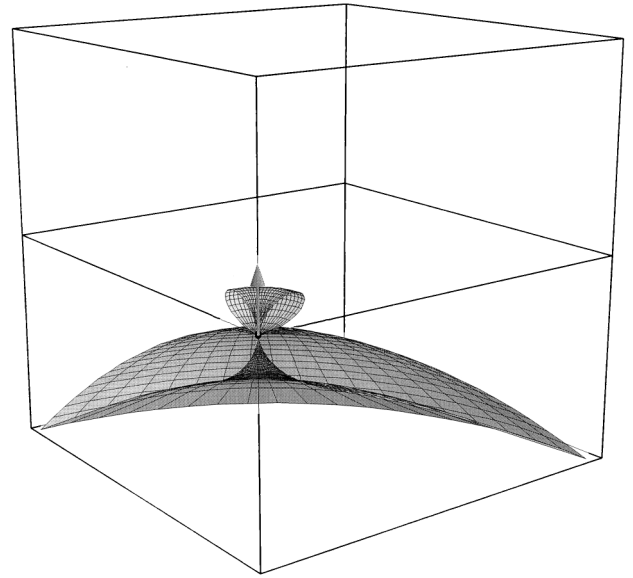
In the special case of a dipole orientation orthogonal to the surface ( $\mathbf{p} = p\hat{z}$ ) one has

$$\begin{aligned} \frac{d^2 S_1}{d\Omega^2} = \frac{cn_1 k_1^2 p^2}{4\pi \epsilon_1^2} q^2 |1 + R_p \exp(2iw_1 z_0)|^2, \\ \frac{d^2 S_2}{d\Omega^2} = \frac{cn_2 k_1^2 w_2^2 p^2}{4\pi \epsilon_1^2 |w_1|^2} q^2 |T_p|^2 \exp[-2 \text{Im}(w_1) z_0], \end{aligned} \quad (23)$$

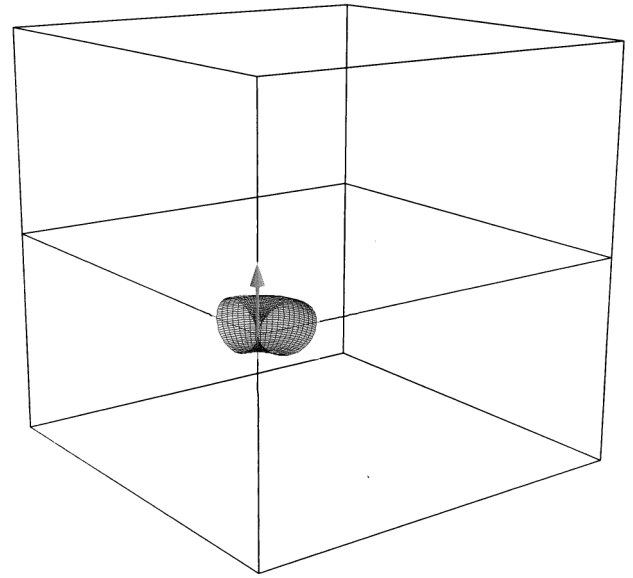
and for a parallel orientation ( $\mathbf{p} = p\hat{x}$ ) one has

$$\begin{aligned} \frac{d^2 S_1}{d\Omega_1^2} = \frac{cn_1 k_0^4 p^2}{4\pi} \left\{ \frac{w_1^2}{k_1^2} \cos^2 \phi |1 - R_p|^2 + \sin^2 \phi |1 + R_s|^2 \right\}, \\ \frac{d^2 S_2}{d\Omega_2^2} = \frac{cn_2 k_0^4 w_2^2 p^2}{4\pi |w_1|^2} \left\{ \frac{|w_1|^2}{k_1^2} \cos^2 \phi |T_p|^2 + \sin^2 \phi |T_s|^2 \right\} \\ \times \exp[-2 \text{Im}(w_1) z_0]. \end{aligned} \quad (24)$$

To demonstrate the meaning of Eqs. (23) and (24), we computed the angular emission distribution of a dipole positioned ( $z = 0$ ) at a water-glass interface ( $n_1 = 1.33$  and  $n_2 = 1.5$ ). For a vertical dipole (where the dipole orientation is perpendicular to the interface) the result is shown in Fig. 2(a), and for the parallel dipole it is in Fig. 3(a). For comparison, in



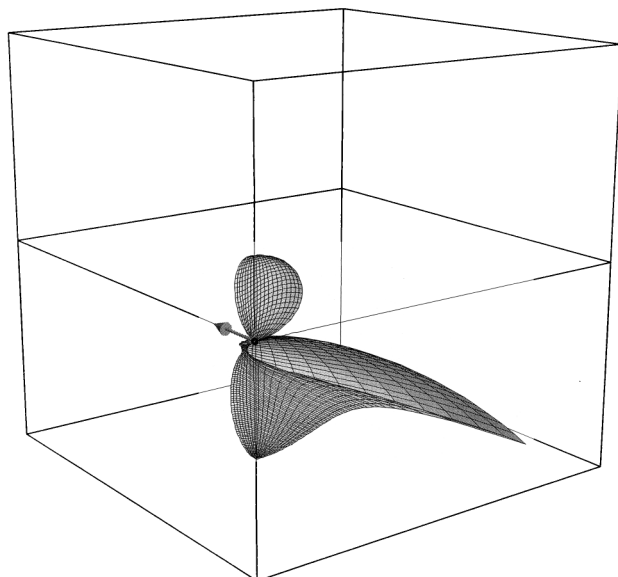
(a)



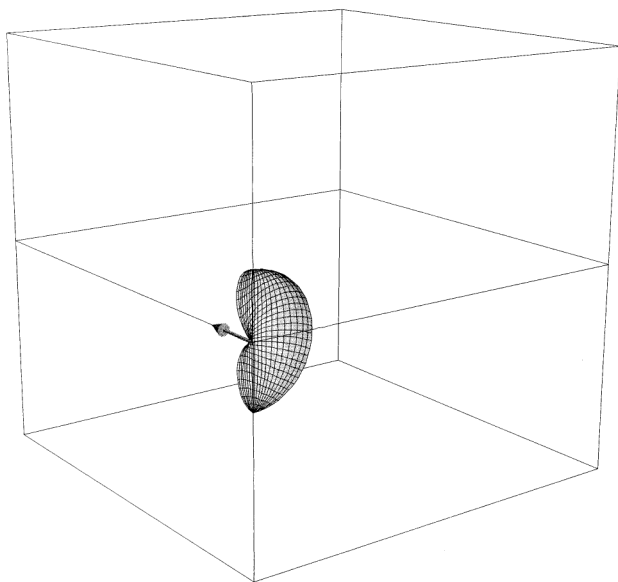
(b)

Fig. 2. (a) Angular distribution of the radiation of an electric dipole with vertical orientation to a surface with refractive index  $n_1 = 1.33$  above the surface and  $n_2 = 1.5$  below it. (b) As in (a) but with  $n_1 = n_2 = 1.33$ .

Figs. 2(b) and 3(b), the emission distributions of a free dipole in water are shown (with no interface). In all four figures the surrounding box always has the same dimensions, facilitating a quantitative comparison of the emission distributions. For the surface-bound emitter, in both vertical and parallel dipole orientation, the maximum emission lies exactly at the azimuthal angle of total internal reflection. A significant amount of radiation emitted into the glass comes from modes that are evanescent on the water



(a)



(b)

Fig. 3. (a) Angular distribution of the radiation of an electric dipole with parallel orientation to a surface with refractive index  $n_1 = 1.33$  above the surface and  $n_2 = 1.5$  below it. (b) As in (a) but with  $n_1 = n_2 = 1.33$ .

side. It is also obvious that the integrated radiation of the dipole at the interface is greater than that of the free dipole in water, a well-known fact that can be measured as a shortening of the fluorescence lifetime of surface-bound fluorescent molecules. With regard to fluorescence light collection, Figs. 2(a) and 3(a) demonstrate that it is most desirable to have collection optics that are able to collect light advantageously around the peak of the fluorescence emis-

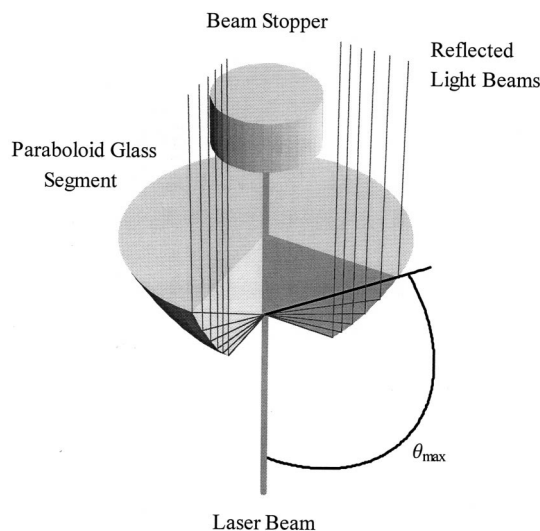


Fig. 4. Schematic of the paraboloid light collector.

sion, that is, around the angle of total internal reflection.

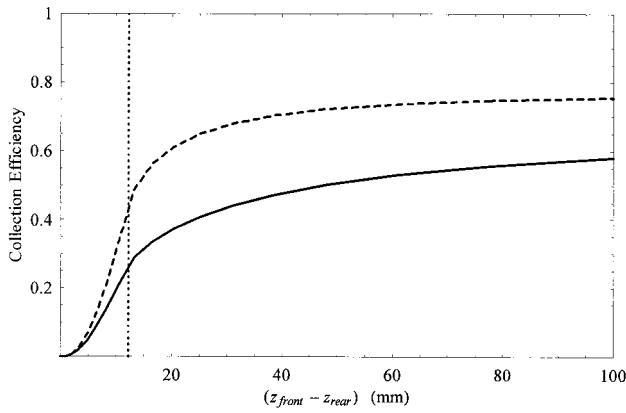
### 3. Paraboloid Light Collector

A schematic representation of the paraboloid light collector is given in Fig. 4. The central element is a body of glass in the shape of a plane-parallel segment of a paraboloid of revolution. Within Cartesian coordinates the equation of the paraboloid segment is given by

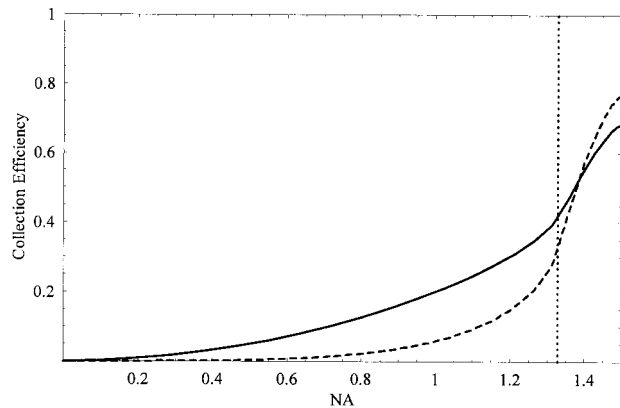
$$z = -\alpha(x^2 + y^2), \quad 0 > z_{\text{front}} \geq z \geq z_{\text{rear}}, \quad (25)$$

where  $\alpha$  is a given constant and the  $z$  axis will be the optical axis of the system. As can be seen, in the chosen coordinate system the paraboloid extends into the negative  $z$  direction. A laser beam is directed along the optical axis onto the front face of the paraboloid segment ( $z = z_{\text{front}} < 0$ ), exciting the fluorescence of molecules bound at that face. The constant  $\alpha$  is chosen in such a way that all light beams emanating from these molecules and hitting the parabolic side wall of the segment are reflected by total internal reflection (the glass-air interface). Thus all the fluorescence light emitted into the glass with azimuthal angles between  $\pi/2$  and some  $\theta_{\text{max}}$  is reflected by the paraboloid into nearly parallel light rays. (For values of  $z_{\text{front}}$  near the value of the paraboloid's geometric focus,  $z_{\text{foc}} = -1/4\alpha$ .)

In Section 4 we show how to focus this light again by a suitable lens arrangement, allowing confocal imaging. Here we study the collection efficiency (CE) of the paraboloid system with respect to the molecule's fluorescence emission characteristics as calculated in Section 2. We suppose that all light rays that are reflected by the parabolic wall can be recollected into a photoelectric detector (see Section 4). Then the CE for a molecule positioned at the front face of the paraboloid segment ( $z = z_{\text{front}}$ ) and sitting



(a)



(b)

Fig. 5. (a) Collection efficiency of the paraboloid light collector for a parallel (solid curve) and vertically (dashed curve) oriented dipole positioned on the optical axis at the front face of the paraboloid segment. The dotted line divides the classical light region (emission angle below the critical angle) on the right side from the evanescent light region (emission angle above the critical angle) on the left side. (b) Collection efficiency of a microscope objective for a parallel (solid curve) and vertically (dashed curve) oriented dipole positioned on the optical axis. The dotted line divides the classical light region (emission angle below the critical angle) on the left side from the evanescent light region (emission angle above the critical angle) on the right side.

on the symmetry axis ( $x, y = 0$ ) is given by the integral

$$CE = 2\pi \int_{\pi/2}^{\theta_{\max}} d\theta \sin \theta \left( \frac{d^2 S_2}{d\Omega_2^2} \right), \quad (26)$$

where the upper integration limit is determined by

$$\theta_{\max} = \frac{\pi}{2} + \arctan \left[ \frac{z_{\text{front}} - z_{\text{rear}}}{|z_{\text{rear}}/\alpha|^{1/2}} \right]. \quad (27)$$

To illustrate the CE of the paraboloid segment, we calculated the CE for a segment with the following parameters:  $\alpha = 0.035$ ,  $z_{\text{front}} = z_{\text{foc}} = -1/4\alpha$ . In Fig. 5(a) we show the dependence of the CE on the value of  $z_{\text{rear}}$ . For comparison we plot [Fig. 5(b)] the

dependence of the CE for a conventional oil immersion microscope objective on its NA as calculated by

$$CE = 2\pi \int_{\theta_{\min}}^{\pi} d\theta \sin \theta \left( \frac{d^2 S_2}{d\Omega_2^2} \right), \quad (28)$$

where the lower integration limit is given by

$$\theta_{\min} = \pi - \arcsin \left( \frac{NA}{n_g} \right), \quad (29)$$

where  $n_g$  denotes the refractive index of glass/immersion oil, which is supposed equal 1.5. In both Figs. 5(a) and 5(b) we plotted separately the case of a vertical (dipole orthogonal to the water-glass interface) and a parallel (dipole parallel to the water-glass interface) dipole orientation. For fluorescing tags on surface-bound macromolecules (e.g., antibodies), which one can assume have the ability to rotate freely in space, the CE will be a weighted sum of the two curves (one-third vertical orientation plus two-thirds parallel orientation). For planar fluorescent molecules (e.g., rhodamine, coumarin, and cyanine dyes) directly adsorbed to the surface the emission dipole orientation is mainly parallel to the surface.<sup>8,9</sup>

In Fig. 5(a) all curves are normalized to the total emission of a dipole with corresponding orientation. Thus in Fig. 5(b) the values of the CE curves at the right box wall are equal to the relative amounts of emission radiated into the glass with respect to the total dipole emission. (An objective with a NA value equal to the refractive index of the glass will collect all the light emitted into the glass.) It can be seen that the relative dipole emission into the glass is greater than half of its total emission for a vertical dipole orientation, even more so than for the parallel dipole orientation.

The main difference between a microscope objective and the paraboloid collector is that the latter collects first, with an increasing value of  $z_{\text{front}} - z_{\text{rear}}$ , the evanescent light modes, whereas the objective collects first, with increasing NA, the nonevanescent light modes. Thus the paraboloid collector is especially advantageous in the case of a vertical dipole axis [dashed curves in Figs. 5(a) and 5(b)], where the emission intensity is significantly concentrated around the angle of total internal reflection. This also explains the crossing of the CE curves in the case of a microscope objective. Only when the NA of the objective is large enough to sample efficiently the evanescent modes ( $NA > 1.33$ ) also can the concentration of the vertical dipole's emission intensity around the angle of total internal reflection exert influence on the overall CE. Comparing Fig. 5(a) with Fig. 5(b), one must also take into account that these figures reflect only the ideal case of lossless optical systems. No reflection losses at the optical interfaces were taken into account. But it is a well-known fact that high-aperture objectives, usually consisting of multiple-lens arrangements, can have significant losses due to reflections at the multiple-lens interfaces. Taking into account that only one

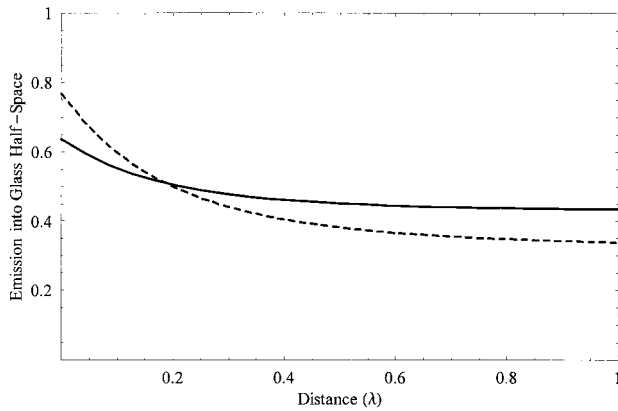


Fig. 6. Total emission of a parallel (solid curve) and vertically (dashed curve) oriented dipole into the glass half-space ( $n_2 = 1.5$ ), depending on its distance from the glass surface. The refractive index of the half-space over the glass surface is equal to  $n_1 = 1.33$  (water).

surface of the paraboloid (the rear surface) causes reflection losses, the ratio of the real CE of the paraboloid collector to that of a high-aperture objective will be rather better than that deduced from Figs. 5(a) and 5(b) alone.

Another important property of the paraboloid collector is the dependence of the CE on the distance of the fluorescing molecules from its surface. In Fig. 6 the dependence of the CE for a vertical and parallel dipole on the dipole's distance from the segment's front face is shown. Both curves are again normalized by the total light emission of a dipole at  $z = z_{\text{front}}$ . As can be seen, the CE falls rapidly, after a distance of only half of the wavelength, near its values at  $z = \infty$ . (Only nonevanescient modes are collected.) Thus the paraboloid collector detects surface-bound molecules significantly better than molecules far from its surface, which is advantageous in surface-sensing applications.

#### 4. Refocusing and Confocal Detection

In Section 3 we studied the CE of the paraboloid collector for a fluorescence source at the focus of the paraboloid. Here we consider two questions: How does one focus light emanating from the paraboloid collector onto a photoelectric detector? How does one reject scattered light emanating at positions different from the fluorescence source position (thus restricting the detection volume)? The latter is an especially significant question because, when extremely low fluorophore surface concentrations are approached, the most efficient light collection becomes useless if one is not able to reject scattered light efficiently. This can best be seen in the limiting case of a single molecule: Where the fluorescence light intensity emanating from a single molecule will not change when the efficient detection volume is increased, the collected intensity of scattered light increases in directly proportion to that volume (see, e.g., Ref. 10). Thus minimizing the de-

tection volume is of utmost importance in ultrasensitive fluorescence-detection systems.

A straightforward way to refocus light reflected by the paraboloid segment is by means of a single spherical lens. If the paraboloid segment's front face is

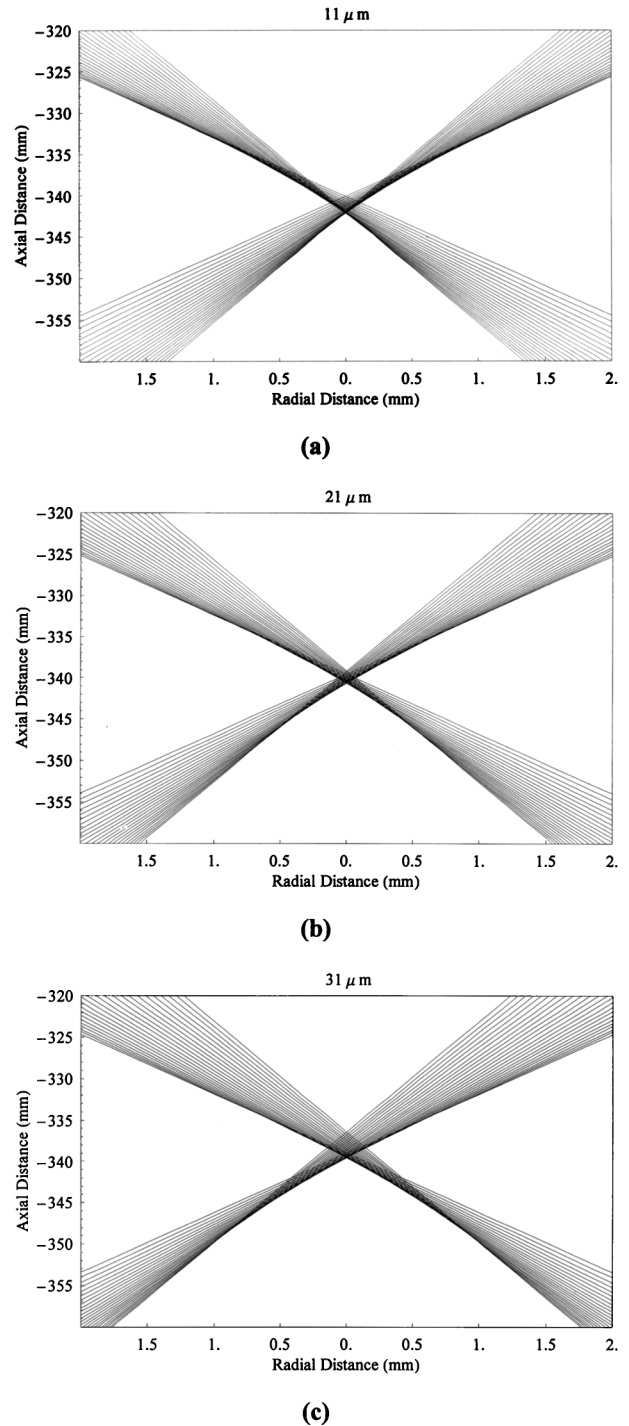


Fig. 7. (a) Paths of light rays near the focus of the focusing lens for a fluorescing source on the optical axis and on the front face of the paraboloid segment, with the front face at position  $z_{\text{front}} = -11 \mu\text{m}$ . (b) As in (a) but with the front face at position  $z_{\text{front}} = -21 \mu\text{m}$ . (c) As in (a) but with the front face at position  $z_{\text{front}} = -31 \mu\text{m}$ .

located exactly at the plane of the paraboloid focus ( $z_{\text{front}} = z_{\text{foc}}$ ), the light rays emanating from that focus leave the collector as perfectly parallel rays with respect to the optical axis. Owing to the spherical aberration of spherical lenses, it is difficult to refocus the light into a single spot, which is important not only for confocal imaging (see below) but also for using photoelectric detectors such as single-photon avalanche diodes that usually have very small active areas (approximately  $100\text{--}200\ \mu\text{m}^2$ ). However, shifting the front face of the paraboloid segment slightly out of the plane of the paraboloid's focus, one can almost completely compensate for the spherical aberration effects of the focusing lens. To demonstrate this, we performed a ray-tracing calculation for a paraboloid segment with  $\alpha = 0.035$  and  $z_{\text{rear}} = 25.15\ \text{mm}$  and a commercially available symmetric convex lens (Mellet Griot, 01 LDX 223) with the following parameters: focal length, 200 mm; diameter, 100 mm; maximum lens thickness, 16.3 mm; minimal distance between the opposite spherical surfaces, 3.9 mm; refractive index,  $n = 1.5187$ . The center of the lens's front surface was positioned 110 mm behind the rear face of the paraboloid segment.

In Fig. 7 we show the paths of selected light rays emanating at  $x, y = 0$  and  $z = z_{\text{front}}$  near the focus of the lens for different locations  $z_{\text{front}}$  of the front face of the paraboloid segment. As can be seen, a displacement of  $21\ \mu\text{m}$  of the front face almost completely compensates for the spherical aberration of the spherical lens. Indeed all light rays are converging within a spot with a radius of  $80\ \mu\text{m}$ .

To study the possibility of confocal imaging (and thus of restricting the detection volume), we calculated the spatially dependent collection efficiency function (CEF) of the system in which a circular aperture of  $80\text{-}\mu\text{m}$  radius is positioned at the point of maximum convergence of the refocused rays. The value of the CEF at a given point P in the object space is directly proportional to the light intensity that an imagined photoelectric detector behind the circular aperture can see from an isotropic light source situated at point P. The CEF was also calculated by a ray-tracing procedure, thus neglecting any wave optical effects. The result is shown in Fig. 8 as a contour plot. As can be seen, the CEF's falloff is much slower on the glass side than on the water side, because from the water side only nonevanescent modes were supposed to be collected. (The coupling of evanescent light modes out of the thin water layer directly adjacent to the water-glass interface was neglected owing to a negligible layer depth of  $\sim 0.5\ \mu\text{m}$ .) But even on the glass side the CEF falls off to its half-maximum value already at a depth of  $8\ \mu\text{m}$ , which is only slightly larger than the detection volume depths of conventional confocal microscopes.<sup>11</sup> Thus we have shown that with the paraboloid collector, not only highly efficient fluorescence collection is possible but also confocal restriction of the detection volume, which is important when one is detecting extremely low fluorophore surface concentrations down to the single-molecule level.

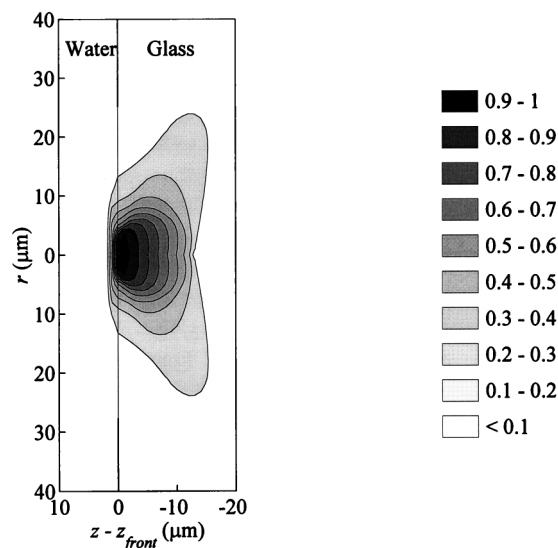


Fig. 8. Spatial dependence of the CEF for a paraboloid plus lens system as described in the text. The paraboloid front face position is set equal to  $z_{\text{front}} = -21\ \mu\text{m}$ . The CEF is normalized by its maximum value.

## 5. Conclusion

We have presented a detailed theoretical study of a new highly efficient light-collecting optical system for applications in highly sensitive fluorescence detection. We have proved not only that the system is able to collect the fluorescence emission of surface-bound molecules with high efficiency but also that it allows for confocal imaging of the detection region, which is of utmost importance for possible applications to problems such as single-molecule detection, where one must insure not only high light-collection capability but also efficient rejection of scattered light. We have shown that very small detection volumes can be achieved by employing a simple off-the-shelf spherical lens. Better results are possible with aspherical or multiple-element lenses. However, such lenses with sufficiently large diameters (200 mm in the present case) are not readily available and usually very expensive (more than \$1000). An apparent drawback of the proposed system is that the paraboloid glass segment also serves as a substrate. However, in a practical realization one can use coverslips as a substrate that is placed on the paraboloid's front face with index-matching immersion oil. Currently, an experimental realization of the system is under way, and we hope to present experimental confirmation of its fluorescence-detection capabilities in a forthcoming paper.

We thank Martin Böhmer (Regensburg University) for many helpful discussions. We are grateful to Richard Ansell (Regensburg University) for linguistic support.

## References

1. R. R. Chance, A. Prock, and R. Silbey, "Molecular fluorescence and energy transfer near interfaces," in *Advances in Chemical*

- Physics*, I. Prigogine and S. R. Rice, eds. (Wiley, New York, 1978), pp. 1–65.
2. W. Lukosz and R. E. Kunz, "Light emission by magnetic and electric dipoles close to a plane interface. I. Total radiated power," *J. Opt. Soc. Am.* **67**, 1607–1615 (1977).
  3. B. Hecht, D. W. Pohl, H. Heinzelmann, and L. Novotny, "'Tunnel' near-field optical microscopy: TNOM-2," *Ultramicroscopy* **61**, 99–104 (1995).
  4. A. Sommerfeld, *Partielle Differentialgleichungen der Physik* (Akademische Verlagsges., Leipzig, 1966), Chaps. 32–33, pp. 226–243.
  5. C. Girard and A. Dereux, "Near-field optics theory," *Rep. Prog. Phys.* **59**, 657–699 (1996).
  6. C. Girard and A. Dereux, "Optical spectroscopy of a surface at the nanometer scale: a theoretical study in real space," *Phys. Rev. B* **49**, 11,344–11,351 (1994).
  7. J. D. Jackson, "Reflection and refraction of electromagnetic waves at a plane interface between dielectrics," in *Classical Electrodynamics* (Wiley, New York, 1975), Chap. 7.3, pp. 278–282.
  8. A. L. Huston and C. T. Reimann, "Photochemical bleaching of absorbed rhodamine 6G as a probe of binding geometries on a fused silica surface," *Chem. Phys.* **149**, 401–407 (1991).
  9. M. Lieberherr, C. Fattinger, and W. Lukosz, "Optical environment-dependent effects on the fluorescence of sub-monomolecular dye layers on interfaces," *Surf. Sci.* **189/190**, 954–959 (1987).
  10. R. A. Keller, W. P. Ambrose, P. M. Goodwin, J. H. Jett, J. C. Martin, and M. Wu, "Single-molecule fluorescence analysis in solution," *Appl. Spectrosc.* **50**, 12–32A (1996).
  11. S. W. Hell, G. Reiner, C. Cremer, and E. H. K. Stelzer, "Aberrations in confocal fluorescence microscopy induced by mismatches in refractive index," *J. Microsc.* **169**, 391–405 (1993).